Journal Pre-proof

Optimisation of adhesive-free high-frequency miniature class IV transducers incorporating single-element piezoelectric plates

Xuan Li, Yifei Wang, Youheng Zeng, Dongliang Shi, Zhihong Huang, Kwok-Ho Lam

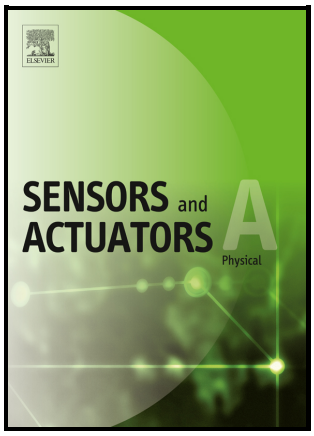

PII: S0924-4247(26)00040-3

DOI: https://doi.org/10.1016/j.sna.2026.117489

Reference: SNA117489

To appear in: *Sensors and Actuators: A. Physical*

Received date: 9 October 2025
Revised date: 31 December 2025
Accepted date: 10 January 2026

Please cite this article as: Xuan Li, Yifei Wang, Youheng Zeng, Dongliang Shi, Zhihong Huang and Kwok-Ho Lam, Optimisation of adhesive-free high-frequency miniature class IV transducers incorporating single-element piezoelectric plates, *Sensors and Actuators: A. Physical,* (2026) doi:https://doi.org/10.1016/j.sna.2026.117489

Optimisation of adhesive-free high-frequency miniature class IV transducers incorporating single-element piezoelectric plates

Xuan Li[1], Yifei Wang[2], Youheng Zeng[3], Dongliang Shi[4], Zhihong Huang[3], and Kwok-Ho Lam[2]

[1]Department of Mechanical Engineering, School of Engineering, University of Southampton, UK
[2]Centre for Medical & Industrial Ultrasonics, James Watt School of Engineering, University of Glasgow, UK
[3]School of Physics, Engineering and Technology, University of York, UK

[4]Alpha Thermoelectric Energy Solutions Co. Ltd, Hong Kong

Abstract — Tissue biopsy under regional anaesthesia requires accurate localisation of the needle tip during penetration through skin and soft tissue. To enhance needle tip visibility in colour Doppler imaging, ultrasonically actuated needle systems based on bolted Langevin transducers have been developed. However, these systems impose design constraints as the needle length must be tuned to the transducer resonance, and their relatively large size limits the suitability for hand-held procedures. Flextensional transducers offer a compact alternative, enabling large displacement with minimal bulk piezoelectric material. This paper presents an optimisation study of three metal shell geometries for class IV miniature flextensional transducers, excited by hard piezoelectric plates to maximise displacement amplification. The transducers employ a negative interference fit between the piezoelectric plate and metal shell, introducing structural pre-stress without bonding or transition mechanisms. Additionally, the dynamic response and power density of the transducers are evaluated for different active materials, including piezoceramics (Pz54) and piezocrystals (Mn:PIN-PMN-PT). Experimental results show that, for identical dimensions, the Mn:PIN-PMN-PT transducer achieves a lower resonant frequency, reduced and near-resistive impedance, enhanced electromechanical coupling, higher mechanical *Q*, and increased power density compared with the piezoceramic counterpart.

Keywords—Class IV flextensional transducer, hard PZT, Mn:PIN-PMN-PT

1. Introduction

Diagnosis and local therapy are often performed using tissue biopsy under regional anaesthesia, facilitated by the percutaneous insertion of a needle into the target site through minimally invasive intervention [1]–[4]. To minimize the risk of damage to surrounding tissues as the needle passes through multiple layers of skin and soft tissue, enhanced visibility is crucial, enabling surgeons to precisely track the position of the needle. As originally reported in [5], colour Doppler imaging of a vibrating needle can significantly improve the visibility. This finding has since driven the development of ultrasonically actuated needle systems, combined with ultrasound-guided imaging, to enhance the needle visibility for both diagnostic and therapeutic procedures [1], [6].

Bolted Langevin transducer (BLT) configuration is commonly used to generate and transmit ultrasonic vibrations to the needle tip. However, the length of the needle must be precisely tuned to resonate at the same frequency as the BLT, typically ranging from 20 to 60 kHz. This requirement poses

Corresponding author: Dr. Kwok-Ho Lam
(email: KwokHo.Lam@glasgow.ac.uk Tel: (+44)(0)7397 865586)

design constraints, potentially leading to reduced efficiency and shifts in resonant frequency as the exposed needle length varies. Furthermore, BLT-based needle systems are often bulky, limiting their ergonomics for hand-held surgical applications.

Flextensional transducers (FTs) have emerged as a promising alternative to the traditional BLTs. Traditionally employed in low- to medium-frequency, high-power acoustic projectors, FTs generate sound through the flexural motion of a metal shell excited by a drive stack operating in an extensional vibration mode [7]. FTs can generally be categorised into seven classes based on the design patterns [7]. Among these, class IV is the simplest and most commonly used configuration, consisting of an elliptical shell driven along its major axis by a piezoelectric or magnetostrictive stack, resulting in amplified motion along the perpendicular axis. Compared to bulk piezoelectric materials, FTs produce significantly larger displacement amplitudes under the same excitation, making them particularly effective in enhancing needle visibility.

The conventional approach to fabricate a class IV FT typically involves either using a transition structure to connect a piezoelectric element to a metal shell [8], [9], [10], or employing epoxy resin as a bonding agent to attach metal end-caps to the piezoelectric element [11]. However, in neither case, the piezoelectric element is subjected to external pre-stress from the metal shell or end-cap, limiting its ability to achieve large displacement amplitudes in the extensional direction. Another drawback of this fabrication method is that the piezoelectric element may not remain securely in place, particularly under continuous and high excitation. Additionally, the bonding agent is prone to softening or cracking at high excitation voltages [12].

To improve the dynamic performance of the class IV FTs, extensive research has been conducted, including studies on various

metal shell or end-cap geometries [8], [10], [13], as well as different configurations of piezoelectric elements, such as bars, plates, disc/ring stack, and conformal driving stacks [11], [14], [15]. To increase structural compliance, grooves have been introduced into the metal shell design [8]. Despite these advances in metal shell design and the exploration of diverse piezoelectric element shapes as the vibration generators, the use of more advanced piezoelectric materials, such as piezocrystal, remains limited.

Recently, relaxor-based single crystals, particularly the third generation manganese-doped $P_b(In_{1/2}Nb_{1/2})O_3$-$Pb(Mg_{1/3}Nb_{2/3})O_3$-$PbTiO_3$ (Mn:PIN-PMN-PT) [16]–[18], have emerged as a promising material for high-power ultrasonic applications. Their ultra-high piezoelectric coefficients (d_{33} > 2000 pC/N), electromechanical coupling factors ($k_{33} > 0.9$), and high mechanical Q ($Q_m \sim$ 1000), make them well-suited for designing miniature high-power devices [19], [20], [21]. However, despite these advantages, a key limitation of Mn:PIN-PMN-PT is the significantly lower tetragonal-to-rhombohedral phase transition temperature, T_{RT}, ([001], $T_{RT} \sim 90 – 120$ °C) compared to the PZTs, which have a Curie temperature (T_C) of approximately 200 – 300 °C [19], [20], [21]. This low transition temperature narrows the range of operation, particularly under high-voltage excitation, leading to increased piezoelectric losses and temperatures.

Although research on incorporating Mn:PIN-PMN-PT material into FTs is limited, a few studies have highlighted its positive impacts on device performance. Notably, Mn:PIN-PMN-PT has demonstrated an approximately 30% increase in bandwidth and a higher transmitting voltage response compared to its hard PZT FT counterpart [10]. Additionally, they have shown an over 50% reduction in heat loss compared to other PIN-PMN-PT and hard PZT actuated FTs [9].

This work presents class IV miniature FTs featuring three different metal shell geometries, designed to optimize the vibration amplifier through structural enhancements. The FTs are fabricated with pre-stress being applied to the piezoceramic plate, leveraging the strength of the metal shell structures. Additionally, vibration responses of the miniature FTs driven by hard PZT ceramics and Mn:PIN-PMN-PT single crystals are compared to evaluate the potential of the new single crystal material for future high-power healthcare applications.

2. Piezoceramic plates

The piezoceramic plate employed in this study is the Pz54 HIFU (CTS Ferroperm Piezoceramics, Kvistgård, Denmark). It features a high mechanical Q factor and low dielectric loss, making it an optimal choice for high-power applications in compact environments, such as therapeutic procedures in confined spaces.

In contrast to the conventional piezoceramic materials, the relaxor-based ferroelectric Mn:PIN-PMN-PT single crystal ([0 0 1]-oriented plate is used in this study) exhibits high piezoelectric performance, including high piezoelectric coefficients, enhanced electromechanical coupling, and high mechanical Q. These characteristics make it particularly advantageous for high-power healthcare applications. Doped with manganese, the mechanical Q of the PIN-PMN-PT single crystal has been greatly improved, while other piezoelectric properties are effectively maintained.

The material properties of the Pz54 and Mn:PIN-PMN-PT plates are presented in Table I. The properties of Pz54 plate are provided by the manufacturer and verified through resonance characterization, while those of Mn:PIN-PMN-PT plate are obtained using a single-sample characterisation method applied to a cube sample poled in the [0 0 1] direction [22], [23]. The characterisation procedure for the Mn:PIN-PMN-PT sample

Table I Material properties of piezoelectric plates

Material	Pz54	Mn:PIN-PMN-PT
Density ρ [kg/m^3]	7760	8120
Relative permittivity ε_{33}^{T}	2800	4510
Dielectric loss factor, tan δ	3.2×10^{-3}	3.3×10^{-3}
Coupling coefficient k_t	0.49	0.69
Coupling coefficient k_{31}	0.34	0.47
Coupling coefficient k_{33}	0.63	0.92
Piezoelectric charge coefficient d_{31} [pC/N]	-201	-553
Piezoelectric charge coefficient d_{33} [pC/N]	479	1520
Elastic compliance coefficient s_{13}^{E} [m^2/N]	-0.689×10^{-11}	-2.652×10^{-11}
Elastic compliance coefficient s_{33}^{E} [m^2/N]	1.86×10^{-11}	2.53×10^{-11}
Mechanical quality factor $Q_{m,t}$	1490	500

follows the method presented in [24].

Compared to the Pz54 ceramics, the Mn:PIN-PMN-PT single crystal exhibits superior material properties, particularly in its high piezoelectric coefficients (d_{31} and d_{33}), dielectric permittivity coefficient (ε_{33}^{T}), and electromechanical coupling coefficients (k_t, k_{31}, and k_{33}). Additionally, the elastic compliance coefficient in the thickness direction (s_{33}^{E}) of the Mn:PIN-PMN-PT single crystal is 36% higher than that of the Pz54 ceramics, while s_{13}^{E} is four times higher. Although the mechanical quality factor ($Q_{m,t}$) associated with the thickness mode of Mn:PIN-PMN-PT is only one third that of Pz54, it remains relatively high among reported single crystals [25], making it advantageous for high-power ultrasonic surgical devices. It should be noted that the miniature FTs

utilize the 31-mode of the piezoelectric plate for excitation, making its parameters particularly relevant for comparison.

3. Miniature flextensional transducers

3.1 Design of metal shells

This study investigates three metal shell geometries made from titanium grade 5 alloy (Ti-6Al-4V), which serve as the vibration amplifiers to augment the mechanical vibration generated from the piezoceramic plate. Given the high cost of the Mn:PIN-PMN-PT material, optimization of the metal shell geometry, aiming to maximize the amplification gain, is conducted exclusively with the Pz54 plates.

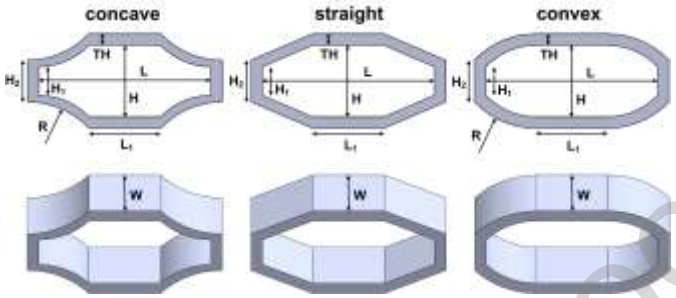

Fig. 1 Three different flextensional metal shell geometries: concave, straight, and convex.

Fig. 1 shows the proposed design of the flextensional metal shell geometries: concave, straight, and convex. The concave shell features four symmetric inward-facing arcs towards the centre, each with a radius (*R*) of 6 mm, while the convex shell has four symmetric outward-facing arcs of the same radius. In contrast, the straight shell exhibits a linear geometry. Dimensions of the metal shells are shown in Table II.

Table II Dimensions of metal shells with varying cavity length *L*

Parameter	Dimension [mm]
Cavity length *L*	9.0 – 14.0
Cavity height *H*	5.0
Cavity top/bottom length L_1	5.0
Cavity left/right height H_1	2.0
Shell left/right height H_2	3.0
Shell thickness *TH*	0.8
Shell radius *R*	6.0
Shell width *W*	5.0

Given the thickness of the Pz54 and Mn:PIN-PMN-PT samples (H_1 = 2 mm), the cavity height (*H*) is set to 5 mm, leaving a 1.5 mm gap on each side once the piezoceramic plates are embedded. Both shell width (*W*) and top/bottom length (L_1) are set to 5 mm. The shell thickness (*TH*) is chosen to be 0.8 mm, making the shell height (H_2) approximately 3 mm. With most dimensions determined for the three metal shells, the cavity length (*L*), which also approximates the length of the piezoelectric plate, is varied from 9 to 14 mm to study the dynamic responses of the FTs to determine the optimal length.

3.2 Fabrication of miniature FTs

The metal shells shown in Fig. 1 were manufactured using wire electrical discharge machining (EDM) technology with a precision of $\pm$10 µm. The cavity length (*L*) of the metal shell was designed to be 0.2 mm shorter than the length of the piezoelectric plate, ensuring pre-stressed through the structural strength. To establish electrical connection, two wires were attached to the top and bottom surfaces of the piezoelectric plates using silver conductive epoxy (8331-14G, MG Chemicals Ltd., Canada).

Fig. 2 Prototypes of the class IV miniature FTs incorporating concave, straight, and convex metal shells, respectively.

Fig. 2 presents the physical prototypes of the miniature FTs incorporating Pz54 plates and various metal shells. The fabrication process involves the use of a precision toolmakers vice to apply pressure in the height (*H*) direction of the three metal shells (shown in Fig. 1), allowing them to expand slightly over 0.2 mm in the length (*L*) direction. The Pz54 plates are inserted into the metal shells, and the vice is then released. This method eliminates the need for epoxy resin between the plate and metal shell, instead, relying on negative interference (structural pre-stress) to achieve a secure bond.

4. Characterisation

All piezoelectric plates and fabricated miniature FTs are characterised through electrical impedance spectra, modal analysis in finite element analysis (FEA), and harmonic response analysis under varying excitation conditions.

4.1 Electrical impedance spectra

The electrical impedance spectra are measured using an impedance analyser (IM3570, Hioki, Japan), with a swept signal of 1 V peak-to-peak. The electromechanical coupling coefficient, k_{eff}, is calculated from the data in impedance spectra using equation (1) [26], providing a quantification of the electromechanical conversion efficiency,

$$k_{\text{eff}}^2 = \frac{f_{\text{a}}^2 - f_{\text{r}}^2}{f_{\text{a}}^2} \tag{1}$$

where $\boldsymbol{f_{\text{a}}}$ represents the anti-resonant frequency and $\boldsymbol{f_{\text{r}}}$ stands for the resonant frequency. The mechanical Q is also calculated using the 3dB bandwidth method for the first length mode (L1, 31-mode) of the plate and for the symmetric vibration mode of the FTs, to study the losses in the materials and devices.

The widely used figure of merit (*FoM*) for an FT, as shown in equation (2), reflects its capability to achieve large displacement amplitudes:

$$\boldsymbol{FoM = Q \cdot k_{\text{eff}}^2} \tag{2}$$

4.2 High excitation vibration analysis

Harmonic analysis experiments are performed to capture the vibration responses of FTs when excited at resonance under increasing voltages. The FT is driven by a frequency sweep, ranging from below to above the resonant frequency, using a burst sine signal generated by a signal generator and amplified by a power amplifier. A 1-D laser Doppler vibrometer (OFV 056, Polytec, Germany) is employed to record the vibration responses on both radiating faces of the FT.

To minimize frequency shifts caused by thermal effects of the piezoceramic plate at high excitation levels, each sine burst signal consists of a fixed 6,000 oscillation cycles, which is sufficient to reach a steady state while minimizing heating. Additionally, a two-second interval between sequential bursts ensures a stable temperature throughout the frequency sweep. Response data are recorded with a resolution of 5 Hz, offering the precision needed to capture detailed variations in the vibration response. The excitation voltage is incrementally increased from 1, then 10 to 100 V (rms) in increments of 10 V, with the amplitude–frequency response measured at each voltage level.

5. Results and discussion

5.1 Determination of the length of piezoelectric plates

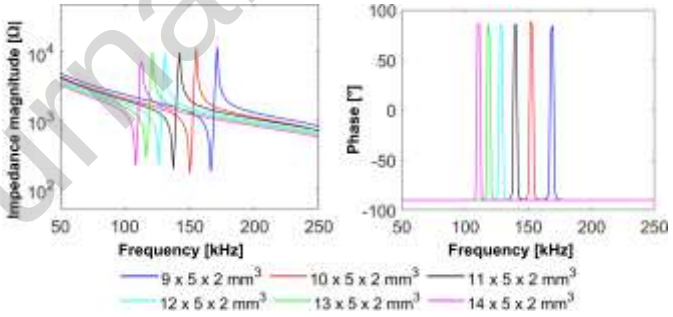

Fig. 3 Impedance and phase characteristics of the Pz54 plates with varying lengths.

The Pz54 sample have lengths ranging from 9 to 14 mm, with a fixed width of 5 mm and a thickness of 2 mm. Both the Pz54 and Mn:PIN-PMN-PT plates used in this study are polarised along the thickness (33) direction, while electromechanical excitation occurs in the 31 direction to drive the metal shells of

Table III Electromechanical characteristics of the Pz54 plates

Dimension [mm^3]	f_{r} [kHz]	f_{a} [kHz]	$Z@f_{\text{r}}$ [Ω]	k_{eff}	Q	*FoM*
9 × 5 × 2	166.41	171.25	178.3	0.236	123	6.85
10 × 5 × 2	150.29	155.13	166.4	0.248	127	7.81
11 × 5 × 2	137.39	142.23	195.6	0.259	99	6.64
12 × 5 × 2	126.10	130.94	225.2	0.269	76	5.50
13 × 5 × 2	116.43	121.26	287.8	0.279	74	5.76
14 × 5 × 2	108.36	113.20	215.1	0.289	66	5.51

the miniature FTs.

Fig. 3 shows the impedance and phase characteristics of the Pz54 plates with different lengths. The first observation is that the resonant frequency of the first length mode (L1, 31-mode) increases linearly as the plate length decreases. However, the impedance magnitude remains approximately a constant at 200 Ω, despite the length variation.

Table III presents the electromechanical characteristics of the Pz54 plates of different lengths at their L1 modes. The electromechanical coupling coefficient k_{eff} increases linearly with the length, while the mechanical Q exhibits an inverse trend to k_{eff}. The figure of merit *FoM* generally decreases with the length, then starts to stabilize once the length exceeds 12 mm.

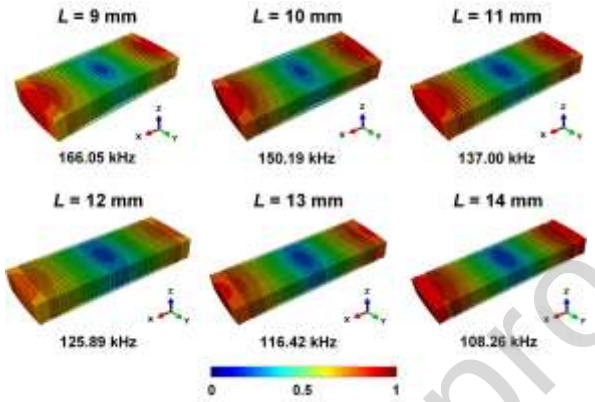

Fig. 4 Simulated L1 vibration mode shapes of the Pz54 plates in FEA with varying lengths. The transition from warm (red) to cool (blue) colours represents anti-nodes to nodes.

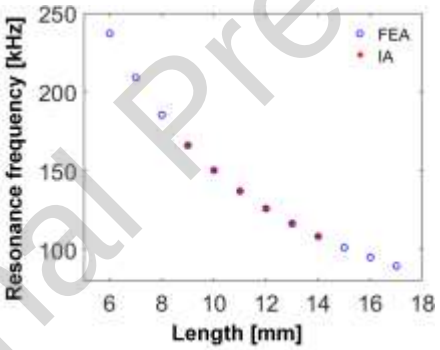

Fig. 5 Simulated and measured L1 mode resonant frequencies as a function of the length of the Pz54 plate.

Fig. 4 presents the simulated vibration mode shapes in finite element analysis (Abaqus-Simulia, Dassault Systèmes, France) as normalized displacement amplitude for the L1 modes of the Pz54 plates with varying lengths. Consistent with the impedance analysis, the resonant frequency of the plates decreases linearly with increasing length, with nodal lines located approximately at the mid-length of the plates.

Fig. 5 compares the simulated and measured resonant frequencies (from the impedance analysis) of the L1 modes of the Pz54 plates with different lengths. The nearly overlapping traces of the simulations and measurements validate the accuracy of the FEA simulation.

Based on the size requirements of the design of the miniature FTs, dimensions of the Pz54 and Mn:PIN-PMN-PT plates are chosen to be $12 \times 5 \times 2$ mm^3.

5.2 Characteristics of the FTs with different metal shell geometries

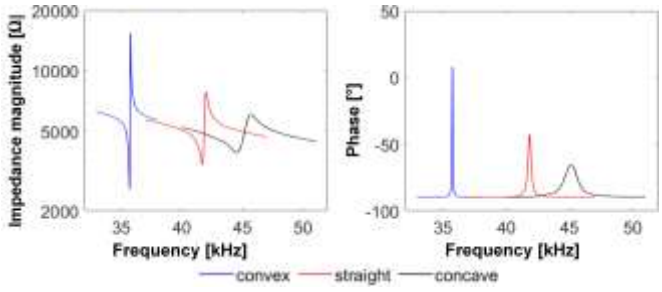

Fig. 6 Impedance and phase characteristics of the miniature FTs incorporating different metal shell geometries and 12 × 5 × 2 mm^3 Pz54 plates.

Fig. 6 presents the impedance and phase characteristics of the miniature FTs fabricated with Pz54 plates and different metal shell geometries (see Fig. 2). The impedance curve of the convex FT shows the lowest resonant frequency and impedance magnitude, the sharpest resonant peak (indicating the highest *Q*), and the narrowest bandwidth (the frequency difference between resonance and anti-resonance). As a comparison, the concave FT exhibits the highest resonant frequency and impedance magnitude, the smoothest resonance peak (indicating the lowest *Q*), and the widest bandwidth.

Based on the phase-frequency curves, all three FTs exhibit strong capacitive characteristics with negative phase angles, except for the convex FT, which crosses 0°. The electromechanical characteristics of these three FTs are summarized in Table IV.

Table IV Electromechanical characteristics of the Pz54 FTs with different metal shell geometries

FT	f_r [kHz]	f_a [kHz]	$Z@f_r$ [Ω]	θ [°]	k_{eff}	Q	FoM
Concave	44.55	45.69	3909	-78	0.222	5	0.246
Straight	41.71	42.00	3413	-66	0.117	35	0.479
Convex	35.71	35.79	2564	-45	0.067	357	1.603

At the same dimensions, the resonant frequency of the convex FT is 35.71 kHz, which is 6 kHz (17%) and 8.84 kHz (25%) lower than that of the concave and straight FTs, respectively. A similar trend is observed for the impedance magnitude: the convex FT exhibits 2.56 kΩ, which is 1.35 kΩ (34%) and 0.85 kΩ (25%) lower than the concave and straight FTs, respectively. Additionally, the phase angle at the resonant frequency of the convex FT is -45°, which is 33° (73%) and 21° (47%) closer to 0° than the concave and straight FTs, respectively. These distinct differences in the impedance magnitude and phase make the convex FT less challenging to excited with a commercial low-output impedance resonance tracking device with an impedance matching circuit.

In terms of the electromechanical coupling coefficient k_{eff}, the concave FT shows the highest value of 0.222, which is twice that of the straight FT and more than three times higher than that of the convex FT. However, the three FTs exhibit significantly difference mechanical *Q* values: the convex FT presents a *Q* that is ten times higher than that of the straight FT and more than seventy times higher than that of the concave FT. This suggests that the concave FT would dissipate the highest amount of energy during excitation. The narrow bandwidth and high-*Q* characteristics of the FTs are attributed to the use of hard piezoelectric material, making them well suited for high-power tissue biopsy needle applications.

To predict which configuration has the potential for generating large displacement amplitudes, *FoM* is calculated. The concave FT shows *FoM* of 0.246, which is half that of the straight FT and nearly one-eighth of the convex FT. This indicates that the convex FT has the potential to generate the highest displacement amplitude at the same excitation.

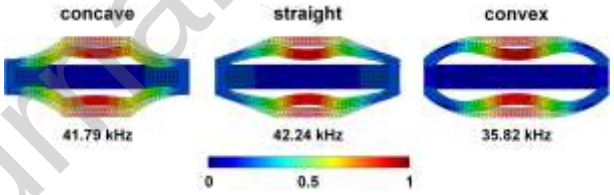

Fig. 7 Simulated symmetric vibration modes of the miniature FTs with different metal shell geometries incorporating 12 × 5 × 2 mm^3 Pz54 plates. The transition from warm (red) to cool (blue) colours represents anti-nodes to nodes.

Fig. 7 shows the side views of the simulated vibration mode shapes as normalized displacement amplitude for the three miniature FTs at their symmetric modes.

At the same dimensions, the convex FT exhibits the lowest resonant frequency, followed by the concave and straight FTs, which show small difference. This observation agrees with the results shown in Fig. 6 and Table IV.

To study the vibration response of the three miniature FTs driven at different excitation levels, the displacement amplitudes as a function of resonant frequency were measured, with the results presented in Fig. 8.

Non-linear softening responses are observed, with discontinuities appearing in all amplitude-frequency curves as the backbone bends to the left [27]. The displacement amplitudes on both top and bottom surfaces of the FTs demonstrate comparable values, confirming a symmetric dynamic behaviour despite the change in excitation. The maximal amplitudes for the concave, straight, and convex FTs are 11, 12.5, and 18.5 μm, respectively, when a 100 V (rms) voltage is applied.

Overall, the convex FT exhibits the optimal performance, characterized by the lowest resonant frequency and impedance magnitude, the highest *FoM* value, a symmetric vibration mode shape, and the largest displacement amplitude, ideally suited for tissue biopsy applications. This shell geometry is therefore selected for the comparison study of the FTs incorporating Pz54 and Mn:PIN-PMN-PT plates.

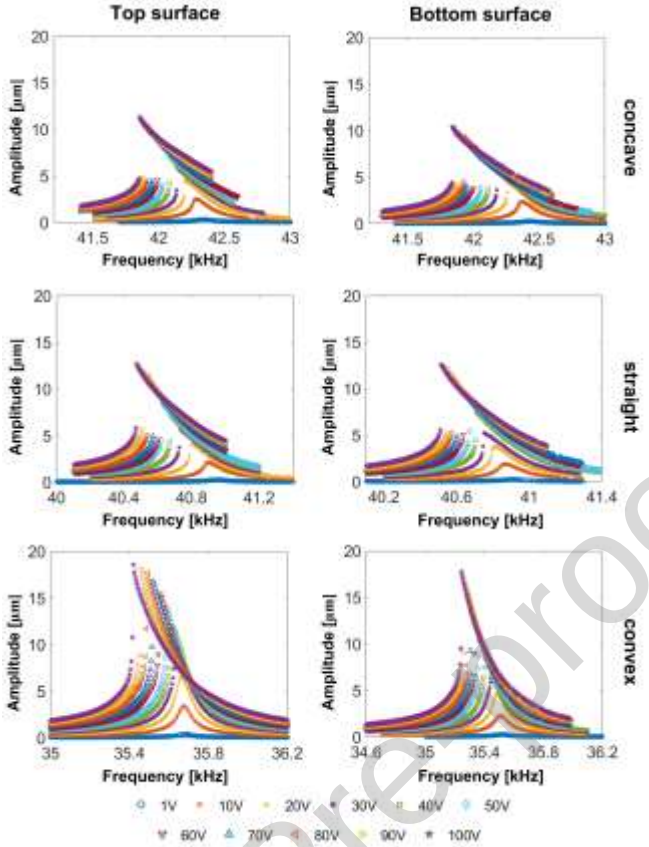

Fig. 8 Amplitude-frequency characteristics of the miniature FTs with different metal shell geometries incorporating 12 × 5 × 2 mm^3 Pz54 plates.

5.3 FTs incorporating Pz54 and Mn:PIN-PMN-PT plates

Since the convex shape has been identified as the optimal metal shell geometry, two new miniature class IV FTs incorporating Pz54 and Mn:PIN-PMN-PT plates (12 × 5 × 2 mm^3) are fabricated for the comparison study.

5.3.1 Characterisation of the Pz54 and Mn:PIN-PMN-PT plates

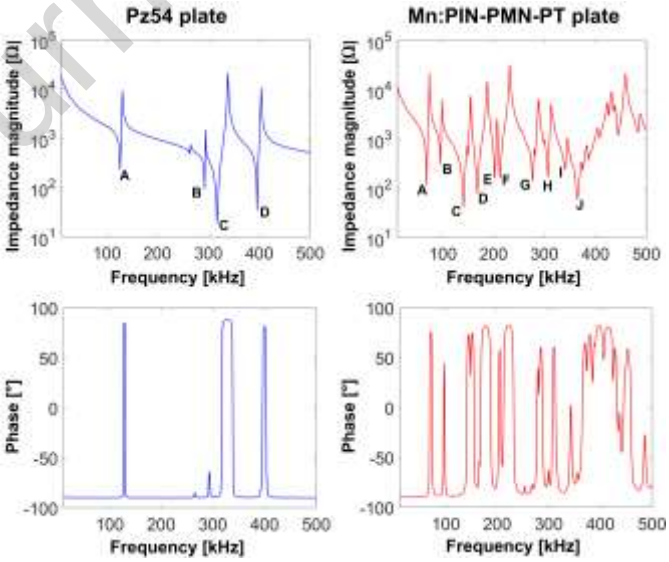

Fig. 9 Impedance and phase characteristics of the 12 × 5 × 2 mm^3 Pz54 and Mn:PIN-PMN-PT plates.

Fig. 9 presents the electrical impedance and phase characteristics of the Pz54 and Mn:PIN-PMN-PT plates. Within a frequency range of 10 to 500 kHz, the Pz54 plate shows four major peaks, labelled as Modes A, B, C, and D. In contrast, the Mn:PIN-PMN-PT plate exhibits a much higher modal density, with more than twelve peaks identified. Considering the low resonant frequencies and impedance magnitudes, only the first ten peaks are analyzed.

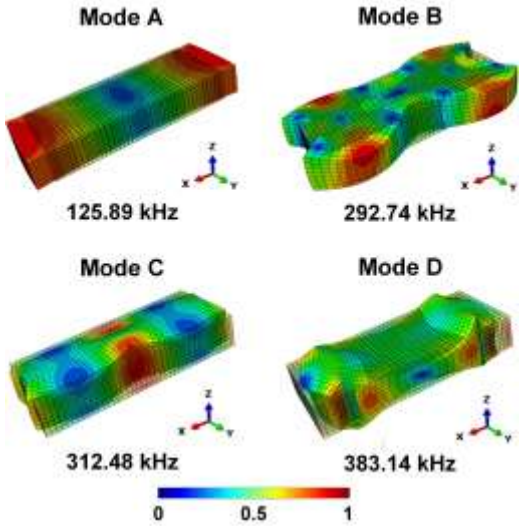

Fig. 10 Simulated vibration mode shapes of the $12 \times 5 \times 2$ mm^3 Pz54 plate. The transition from warm (red) to cool (blue) colours represents anti-nodes to nodes.

The simulated vibration mode shapes, represented as normalized displacement amplitudes of the Pz54 and Mn:PIN-PMN-PT plates are presented in Fig. 10 and Fig. 11, respectively. It should be noted that full material property matrices are employed to simulate the vibration behaviour of both the Pz54 and Mn:PIN-PMN-PT plates. In particular, for Mn:PIN-PMN-PT, the complete material property matrix is constructed by combining the parameters shown in Table I with the remaining properties taken from [24].

For the Pz54 plate shown in Fig. 10, Mode A exhibits dominant motion in the X direction, which is identified as the L1 mode at around 126 kHz. For Mode B and Mode C, the vibration mode shapes indicate width-dominant motions at around 300 kHz. Mode D resembles closely the complex third length mode (L3) at a resonant frequency slightly under 400 kHz.

Similar to the Pz54 plate, Mode A of the Mn:PIN-PMN-PT plate exhibits the largest amplitude in the X direction, which is identified as the L1 mode (see Fig. 11). However, the resonant frequency is approximately 69 kHz, which is almost half of the resonant frequency of the L1 mode of the Pz54 plate. This difference is mainly due to the significantly higher elastic compliance and piezoelectric charge coefficients of the Mn:PIN-PMN-PT material. Mode D displays a similar vibration mode shape but at half the frequency (163 kHz) compared to Mode B of the Pz54 plate. Mode E represents the L3 mode at around 210 kHz, which is comparable to Mode D of the Pz54 plate at around 400 kHz. Mode F to Mode J are higher-order complex vibration modes which are not present for the Pz54 plate.

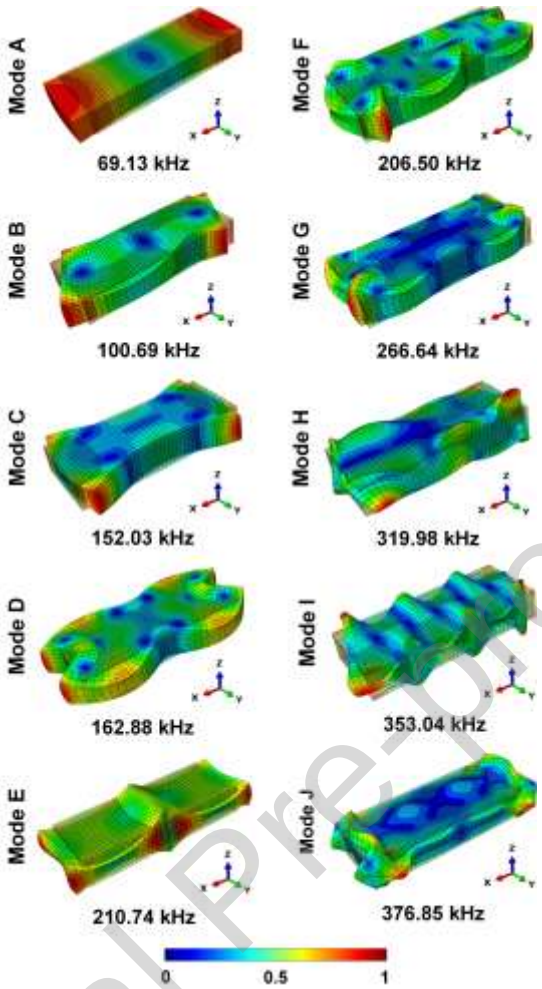

Fig. 11 Simulated vibration mode shapes of the $12 \times 5 \times 2$ mm^3 Mn:PIN-PMN-PT plate. The transition from warm (red) to cool (blue) colour represents anti-nodes to nodes.

5.3.2 Characterisations of the FTs incorporating Pz54 and Mn:PIN-PMN-PT plates

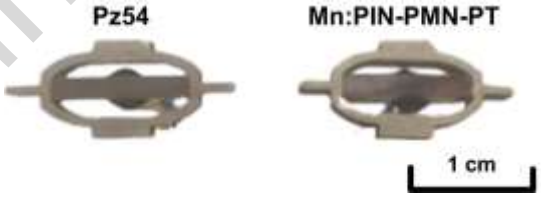

Fig. 12 Fabricated class IV miniature FTs incorporating Pz54 and Mn:PIN-PMN-PT plates.

With full characterisation of the Pz54 and Mn:PIN-PMN-PT plates and identification of the L1 modes, the miniature FTs incorporating both plates have been fabricated, which are shown in Fig. 12.

The fabrication process follows the procedures outlined in Section 3.2. However, the thickness of the convex metal shells (*TH*, see Table II) has been increased from 0.8 to 0.9 mm to explore the effect on the resonant frequency and displacement amplitude. Additionally, two symmetric flanges, each has 2.8 mm in length, 5 mm in width (matching the width of the metal shell), and 0.8 mm in thickness, have been manufactured at both sides of the metal shells for fixturing purposes.

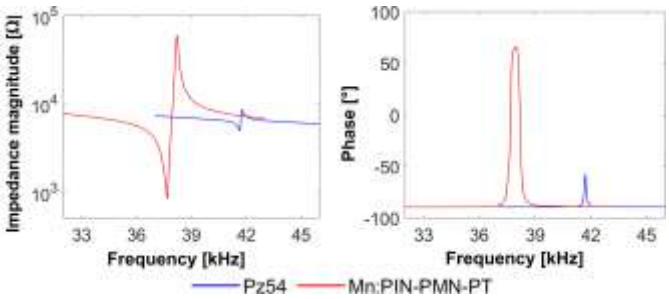

Fig. 13 Impedance and phase characteristics of the miniature Pz54 and Mn:PIN-PMN-PT FTs.

Fig. 13 shows the impedance and phase characteristics of the FTs incorporating Pz54 and Mn:PIN-PMN-PT plates. The electromechanical parameters are summarized in Table V.

The impedance curves of the Mn:PIN-PMN-PT devices clearly show significantly lower impedance magnitudes compared to the Pz54 device. Furthermore, the phase of the Mn:PIN-PMN-PT device crosses 0°, different from the strong capacitive characteristics observed for the Pz54 device. This difference would significantly simplify the design and implementation of an impedance-matching circuit when driving the Mn:PIN-PMN-PT device continuously with a commercial resonance tracking apparatus.

Table V Electromechanical characteristics of the FTs incorporating Pz54 and Mn:PIN-PMN-PT plates

FT	Pz54	Mn:PIN-PMN-PT
f_r [kHz]	41.64	37.69
f_a [kHz]	41.75	38.22
Z [Ω]	4908	842
θ [°]	-75	5
k_{eff}	0.07	0.17
Q	12	314
FoM	0.06	8.65

From Table V, the impedance magnitude of the Pz54 FT is nearly six times higher than that of the Mn:PIN-PMN-PT FT. The phase angles are -75° (strong capacitive) for the Pz54 FT and 5° (nearly resistive) for the Mn:PIN-PMN-PT FT. The coupling coefficient k_{eff} of the Mn:PIN-PMN-PT FT is more than double that of the Pz54 device. Regarding mechanical Q and *FoM*, the Mn:PIN-PMN-PT FT (314, 8.65) is more than an order of magnitude higher and over one hundred times larger than the Pz54 device (12, 0.06), respectively.

In summary, the electromechanical characteristics of the Mn:PIN-PMN-PT device demonstrate exceptional values compared to the Pz54 device, particularly with respect to the significantly higher mechanical Q and *FoM*. These results make the Mn:PIN-PMN-PT material especially attractive for use in the flextensional configurations.

To investigate the vibration mode shapes of the FTs incorporating Pz54 and Mn:PIN-PMN-PT plates, FEA simulation using normalized displacement amplitude is performed, and the results are presented in Fig. 14.

With the same dimensions, the resonant frequency of the Pz54 FT is around 24% higher than that of the Mn:PIN-PMN-PT FT, which is mainly due to the significantly higher elastic compliance of the Mn:PIN-PMN-PT material at the 31 direction (see Table I).

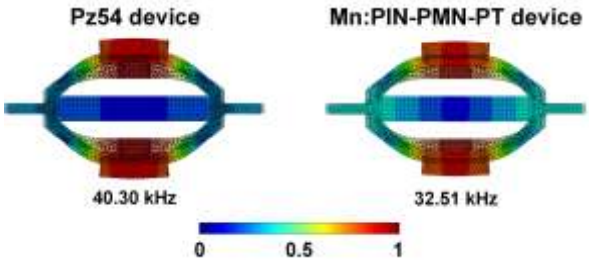

Fig. 14 Simulated vibration mode shapes of the Pz54 and Mn:PIN-PMN-PT FTs. The transition from warm (red) to cool (blue) colour represents anti-nodes to nodes.

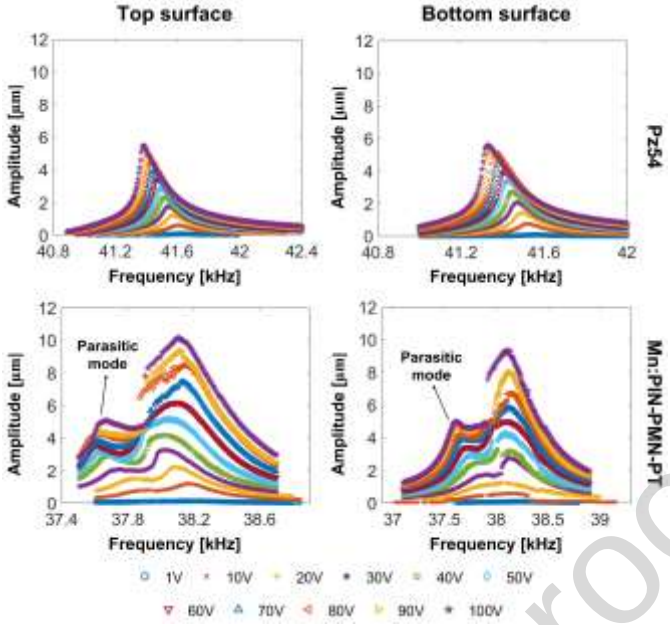

Fig. 15 Amplitude-frequency characteristics of the Pz54 and Mn:PIN-PMN-PT FTs.

Fig. 15 shows the displacement amplitude measured at the top and bottom surfaces of the two FTs across the resonant frequencies at the symmetric modes. The first observation is that the maximum displacement amplitude of the Mn:PIN-PMN-PT FT (10 μm) is nearly double that of the Pz54 FT (6 μm), due to the significantly higher *FoM* value (see Table V). The amplitudes at the top and bottom surfaces of the Pz54 FT show similar values, while the amplitudes at the bottom surface of the Mn:PIN-PMN-PT FT are approximately 1 μm lower than those at the top surface.

Compared to the amplitude of the convex FT shown in Fig. 8, the amplitude of the Pz54 FT in Fig. 15 is approximately 68% lower, because of the increased thickness of the convex metal shell, leading to a reduction in the compliance and an increase in the resonant frequency. Another observation is that the amplitude-frequency characteristics of the Mn:PIN-PMN-PT FT exhibit a parasitic mode near the main resonance peak, which is absent in the low-excitation impedance curves (see Fig. 13). This neighbouring mode may be attributed to the higher elastic compliance of the Mn:PIN-PMN-PT material, causing the 0.2 mm negative interference between the plate and metal shell to potentially be the non-optimal value. Fabrication imperfections, such as the piezoelectric plate being misaligned within the metal shell during structural pre-stress, could also have contributed to the emergence of the parasitic mode.

Additionally, the Mn:PIN-PMN-PT plate was arbitrarily cut from a disc sample (unlike the Pz54 plate extracted from a rectangular sample), and its domain structure was not pre-characterized by X-Ray diffraction (XRD). As a result, misalignment between the orientation of the disc and the domain wall may have further led to the occurrence of the parasitic mode. Another factor contributing to the observed parasitic mode is that the composition of the Mn:PIN-PMN-PT material may lie near or within the morphotropic phase boundary, as suggested by its high piezoelectric charge coefficient d_{33} and high relative permittivity ε_{33}^{T}. This can result in a more complex crystal structure and the possible coexistence of multiple phases within the plate. The formation of such additional phases is particularly likely when the FT is excited at high electric fields. Therefore, to suppress parasitic modes in the device, a crystal composition with a lower PT content is preferred.

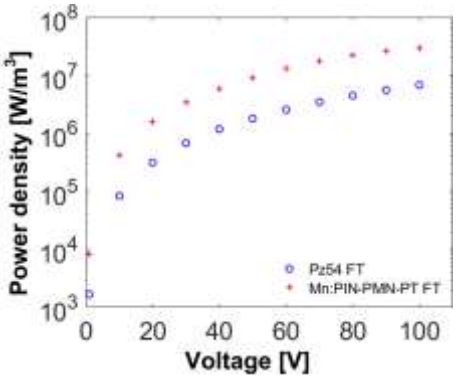

Fig. 16 Power density on a logarithmic scale as a function of the excitation voltage for the Pz54 and Mn:PIN-PMN-PT FTs.

The power density P_d is also calculated for the two FTs using equation (3),

$$P_d = \frac{UI\cos\theta}{V} \quad (3)$$

where U and I are the amplitudes of voltage and current, respectively, θ represents the phase difference between voltage and current, and V is the volume of the piezoelectric plates. Voltage and current signals are measured using the built-in sensors of the power amplifier, and the phase difference between them is calculated using a custom LabVIEW program.

From Fig. 16, the power density, P_d, of the Mn:PIN-PMN-PT FT is four to five times higher than that of the Pz54 FT across all excitation voltages, highlighting the superior capability of the single crystal material in drawing more power from the electric source.

6. Conclusion

This paper presents a novel design of class IV miniature FTs, intended as ultrasonic actuators for driving a percutaneous needle through skin and soft tissue for tissue biopsy applications. To maximise the displacement amplitude and enhance needle visibility, the miniature FTs are fabricated with structural pre-stress of the metal shells. This pre-stress is achieved through applying negative interference between the length of the piezoelectric plate and the void length of the metal shell. As a result, the need for transition mechanism or epoxy resin bonding agents between the piezoelectric plate and the metal shell is eliminated, addressing the common weaknesses and failure risks associated with these materials at high excitation levels.

Among the FTs with three different metal shell geometries, the one with a convex shape shell displays the lowest resonant frequency and impedance magnitude, weaker capacitive characteristic, and the highest *FoM*, resulting in the largest displacement amplitude at the same excitation.

The Mn:PIN-PMN-PT FT generates displacement amplitudes nearly twice as high as the hard piezoceramic FT at the same excitation, primarily due to its significantly higher coupling coefficients k_{eff} and mechanical Q, lower resonant frequency, and lower impedance magnitude. Additionally, compared to the Pz54 FT, the Mn:PIN-PMN-PT FT exhibits significantly higher power density. However, due to the orientation dependence and low stiffness of the Mn:PIN-PMN-PT plate, along with the imperfections in the fabrication process of the miniature FT and possible coexistence of multiple phases within the plate due to high charge coefficient and relative permittivity, the vibration response develops a parasitic mode near the resonance of the symmetric mode, which becomes particularly prominent at high excitation levels. This parasitic mode can significantly reduce the visibility of the needle and may induce complex vibration patterns. Therefore, this study highlights the importance of carefully preparing the piezocrystal plate to ensure symmetric and uniform vibration motion before embedding it into the transducer, as well as adopting an appropriate interference to apply structural pre-stress.

Acknowledgement

The authors thank Alpha Thermoelectric Energy Solutions Co. Ltd for providing the Mn:PIN-PMN-PT materials.

References

[1] Y. Kuang, A. Hilgers, M. Sadiq, S. Cochran, G. Corner, and Z. Huang, "Modelling and characterisation of a ultrasound-actuated needle for improved visibility in ultrasound-guided regional anaesthesia and tissue biopsy," *Ultrasonics*, vol. 69, pp. 38–46, 2016.

[2] V. Dremin, E. Potapova, E. Zherebtsov, K. Kandurova, V. Shupletsov, A. Alekseyev, A. Mamoshin, and A. Dunaev, "Optical percutaneous needle biopsy of the liver: a pilot animal and clinical study," *Scientific Report*, vol. 10, no. 14200, pp. 1–11, 2020.

[3] H. Bessaguet, P. Calmels, A. Schnitzler, F. Coroian, P. Giraux, F. Angioni, A. Adham, P. Denormandie, R. David, and E. Ojardias, "Percutaneous needle tenotomies: indications, procedures, efficacy and safety. A systematic review," *Annals of Physical and Rehabilitation Medicine*, vol. 67, no. 5, pp. 1–15, 2024.

[4] A. Veltri, I. Bargellini, L. Giorgi, P. A. M. S. Almeida, and O. Akhan, "CIRSE guidelines on percutaneous needle biopsy (PNB)," *CardioVascular and Interventional Radiology*, vol. 40, no. 10, pp. 1501–1513, 2017.

[5] R. Feld, L. Needleman, and B. B. Goldberg, "Use of needle-vibrating device and color Doppler imaging for sonographically guided invasive procedures," *American Journal of Roentgenology*, vol. 168, no. 1, pp. 255–256, 1997.

[6] M. Sadiq, S. Cochran, X. Liao, and Z. Huang, "Enhanced US-guided needle intervention through ultrasound actuation of a standard needle," *IEEE International Ultrasonic Symposium*, pp. 1–4, 2014.

[7] C. H. Sherman and J. L. Butler, "Transducers and arrays for underwater sound," Chapter 1 Introduction, Chapter 3 Transducers as Projectors, *Springer*, 2016.

[8] R. Guo, S. Li, T. Li, X. Sun, L. Lin, and S. Sun, "Analysis and design of low frequency and high power flextensional transducer with double-grooves," *Applied Acoustics*, vol. 149, pp. 25–31, 2019.

[9] R. Guo, S. Li, D. An, T. Han, J. Chen, and W. Cao, "Comprehensive analysis of Mn:PIN-PMN-PT single crystals for Class IV flextensional transducer," *Ceramics International*, vol. 44, no. 3, pp. 2864–2868, 2018.

[10] J. Zheng, S. Li, and B. Wang, "Design and analysis of a broadband class VII flextensional transducer with the third-generation crystal, Mn:PIN-PMN-PT," *Sensors and Actuators A: Physical*, vol. 345, pp. 1–7, 2022.

[11] K.H. Lam, X.X. Wang, and H.L.W. Chan, "Lead-free piezoceramic cymbal actuator," *Sensors and Actuators A: Physical*, vol. 125, no. 2, pp. 393–397, 2006.

[12] F. Bejarano, A. Feeney, and M. Lucas, “A cymbal transducer for power ultrasonics applications,” *Sensors and Actuators A: Physical*, vol. 210, pp. 182–189, 2014.

[13] C. L. Sun, K. H. Lam, H. L. W. Chan, X. Z. Zhao, and C. L. Choy, “A novel drum piezoelectric-actuator,” *Applied Physics A, Materials Science & Processing*, vol. 84, pp. 385–389, 2006.

[14] S. C. Butler, “A directional dogbone flextensional transducer,” *Proceedings of Meetings on Acoustics*, vol. 11, no. 1, pp. 1–24, 2011.

[15] T. Zhou, Y. Lan, Q. Zhang, J. Yuan, S. Li, and W. Lu, “A conformal driving class IV flextensional transducer,” *Sensors*, vol. 18, no. 7, 2018.

[16] X. Qi, E. Sun, J. Wang, R. Zhang, Bin Yang, and W. Cao, “Electromechanical properties of Mn-doped $Pb(In_{1/2}Nb_{1/2})O_3$-$Pb(Mg_{1/3}Nb_{2/3})O_3$-$PbTiO_3$ piezoelectric ceramics,” *Ceramics International*, vol. 42, no. 14, pp. 15332–15337, 2016.

[17] E. Sun, R. Zhang, F. Wu, B. Yang, and W. Cao, “Influence of manganese doping to the full tensor properties of $0.24Pb(In_{1/2}Nb_{1/2})O_3$-$0.47Pb(Mg_{1/3}Nb_{2/3})O_3$-$0.29PbTiO_3$ single crystals,” *Journal of Applied Physics*, vol. 113, no. 7, pp. 1–4, 2013.

[18] H. Wan, C. Luo, C. C. Chung, Y. Yamashita, and X. Jiang, “Enhanced dielectric and piezoelectric properties of manganese-doped $Pb(In_{1/2}Nb_{1/2})O_3$-$Pb(Mg_{1/3}Nb_{2/3})O_3$-$PbTiO_3$ single crystals by alternating current poling,” *Applied Physics Letters*, vol. 118, no. 10, 2021.

[19] S. Zhang, F. Li, X. Jiang, J. Kim, J. Luo, and X. Geng, “Advantages and challenges of relaxor-$PbTiO_3$ ferroelectric crystals for electroacoustic transducers - A review,” *Progress in Materials Science*, vol. 68, pp. 1–66, 2015.

[20] S. Zhang and T. R. Shrout, “Relaxor-PT single crystals: Observations and developments,” *IEEE Transactions on Ultrasonics, Ferroelectrics, and Frequency Control*, vol. 57, no. 10, pp. 2138–2146, 2010.

[21] R. Sahul, “Effect of manganese doping on PIN-PMN-PT single crystals for high power applications,” *PhD Thesis*, August, 2014.

[22] N. G. Fenu, N. Giles-Donovan, M. R. Sadiq, and S. Cochran, “Full set of material properties of lead-free PIC 700 for transducer designers,” *IEEE Transactions on Ultrasonics, Ferroelectrics, and Frequency Control*, vol. 68, no. 5, pp. 1797–1807, 2021.

[23] S. Li, L. Zheng, W. Jiang, R. Sahul, V. Gopalan, and W. Cao, “Characterization of full set material constants of piezoelectric materials based on ultrasonic method and inverse impedance spectroscopy using only one sample,” *Journal of Applied Physics*, vol. 114, no. 10, pp. 1–7, 2013.

[24] X. Li, N. G. Fenu, N. Giles-donovan, S. Cochran, and M. Lucas, “Can Mn:PIN-PMN-PT piezocrystal replace hard piezoceramic in power ultrasonic devices?,” *Ultrasonics*, vol. 138, pp. 1–16, 2024.

[25] K. Echizenya, N. Noda, and H. Noro, “Characterization of Mn-doped PIN-PMN-PT single crystal grown by continuous-feeding bridgeman method,” *Crystals*, vol. 12, no. 9, pp. 1–8, 2022.

[26] A. Caronti, R. Carotenuto, and M. Pappalardo, “Electromechanical coupling factor of capacitive micromachined ultrasonic transducers,” *The Journal of the Acoustical Socety of America*, vol. 113, no. 1, pp. 279–288, 2003.

[27] A. Mathieson, A. Cardoni, N. Cerisola, and M. Lucas, “Understanding nonlinear vibration behaviours in high-power ultrasonic surgical devices,” *Proceedings of the Royal Socety A: Mathematical, Physical and Engineering Sciences*, vol. 471, no. 2176, pp. 1–19, 2015.

Xuan Li received the B. Sc. degree in mechanical engineering from the Beijing University of Technology, Beijing, China, the M.Sc. degree in mechanical engineering from the Delft University of Technology, Delft, The Netherlands, and the Ph.D. degree in mechanical and manufacturing engineering from Loughborough University, Loughborough, U.K., in 2014. He is currently a Lecturer in Mechanical Engineering at the Department of Mechanical Engineering, at the University of Southampton, Southampton, U.K. His research interests include miniature ultrasonic surgical device development, ultrasonically assisted machining and manufacturing, new generation of piezoelectric materials, nonlinear dynamics and control.

Yifei Wang is currently a Ph.D. student at the Centre for Medical and Industrial Ultrasonics, at the James Watt School of Engineering, at the University of Glasgow, Glasgow, U.K. His research interest is to apply new generation of piezoelectric materials to biomedical imaging for healthcare applications.

Youheng Zeng is currently a Ph.D. student at the School of Physics, Engineering and Technology, at the University of York, York, U.K. His research interest is to develop ultrasonically actuated needle devices and control systems to assist the tissue biopsy processes.

Dongliang Shi received the Ph.D. degree in Department of Electrical Engineering from the Hong Kong Polytechnic University in 2019. During his graduate studies, he worked on processing and characterizations of thermoelectric materials. He has also been working in the field of smart multifunctional materials, such as piezoelectric and magnetoelectric materials, and their applications. His recent research interests include thermoelectric materials, ultrasonic transducer technology, and their sensing and energy harvesting applications.

Zhihong Huang joined the University of York in July 2024 as Professor of Healthcare Engineering in the School of Physics, Engineering and Technology. With a background in instrumentation and mechanical engineering, and over 20 years at the University of Dundee, her research focuses on cross-disciplinary biomedical engineering, particularly medical ultrasound technologies, including imaging, high-intensity ultrasound, and optical coherence tomography–based elastography.

Kwok-ho (Koko) Lam is a Reader in Ultrasonics at the James Watt School of Engineering, University of Glasgow, and an Adjunct Professor in Electrical Engineering at The Hong Kong Polytechnic University. He received his M.Phil. and Ph.D. degrees in Applied Physics from HKPolyU. His research focuses on ultrasound transducer technology for biomedical and non-destructive evaluation applications, materials for energy conversion and storage, and multimodal imaging. He has published over 220 papers and holds multiple granted patents. He has been recognised among the world's top 2% scientists (Stanford University, 2021–2022) and is a Senior Member of IEEE.

The authors declare that they have no known competing financial interests or personal relationships that could have appeared to influence the work reported in this paper

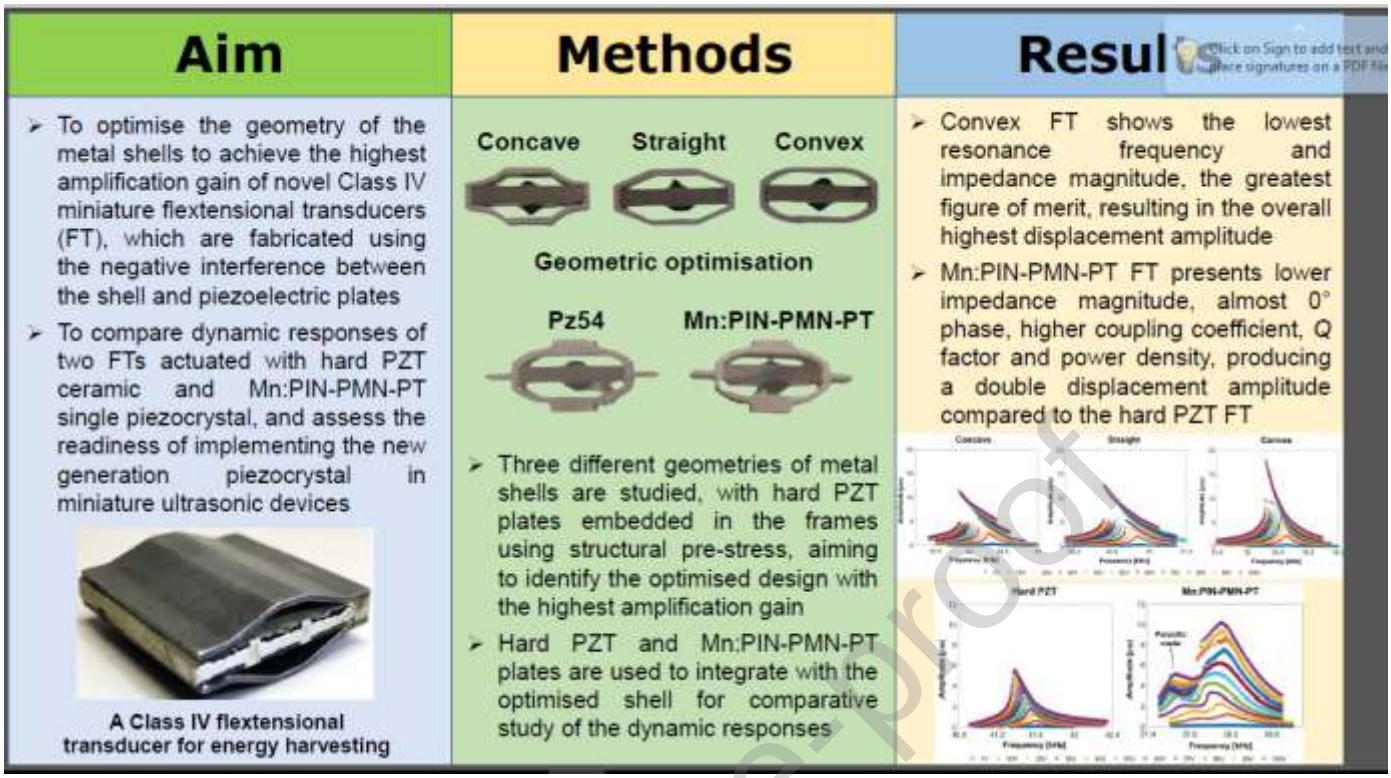

Highlights:

- Miniature FT with convex metal shell develops the largest displacement amplitude.
- Mn:PIN-PMN-PT plate presents more complex vibrational behaviour than the PZT plate.
- Mn:PIN-PMN-PT FT develops two times higher displacement amplitude than the PZT FT.